

# Efficient Cesium Lead Halide Perovskite Solar Cells through Alternative Thousand-Layer Rapid Deposition

Hung-Yu Lin, Chien-Yu Chen, Bo-Wei Hsu, Yu-Lun Cheng, Wei-Lun Tsai, Yu-Ching Huang, Cheng-Si Tsao, and Hao-Wu Lin\*

The novel growth of cesium lead halide perovskite thin films, which are prepared through thousand-layer rapid alternative deposition, is performed by developing an active perovskite film consisting of a layer-by-layer structure. This method is considerably more difficult to be implemented from the solution process. The obtained thin film morphology and characteristics are distinguished from that of the traditional a few layers and two-material codeposition. These alternative deposited perovskites are integrated with vacuum-deposited carrier-transporting layers and electrodes, and all vacuum-sublimed perovskite solar cells exhibit an outstanding power conversion efficiency of 13.0%. The use of these devices for environmental light energy harvesting provides a power conversion efficiency of 33.9% under fluorescent light illumination of 1000 lux.

## 1. Introduction

Halide perovskites have received considerable attention owing to their unparalleled photophysical properties and favorable commercial applications in solar cells, environmental light harvesting devices, and light-emission devices.<sup>[1–7]</sup> Halide perovskites with organic cation are generally fabricated using solution solvents because the process of organic halide formation through vacuum deposition is difficult.<sup>[8–11]</sup> Organic halide precursors exhibited gaseous characteristics because of their small molecular weight and thus were build-up in the complete vacuum chamber. However, by replacing organic halides with cesium halides, the problems related to organic halides in the vacuum process were mostly prevented because of the conventional physical vapor deposition characteristics of cesium halides. This advantage provides new opportunities for developing

H.-Y. Lin, C.-Y. Chen, B.-W. Hsu, Y.-L. Cheng, W.-L. Tsai, Prof. H.-W. Lin  
Department of Materials Science and Engineering  
National Tsing Hua University  
Hsinchu 30013, Taiwan  
E-mail: hwlin@mx.nthu.edu.tw

Prof. Y.-C. Huang  
Department of Materials Engineering  
Ming Chi University of Technology  
New Taipei City 24301, Taiwan  
Prof. C.-S. Tsao  
Institute of Nuclear Energy Research  
Taoyuan 32546, Taiwan

 The ORCID identification number(s) for the author(s) of this article can be found under <https://doi.org/10.1002/adfm.201905163>.

DOI: 10.1002/adfm.201905163

cesium lead halide perovskite thin films through vacuum deposition. Several groups have demonstrated promising solar cell performance and carrier properties of vacuum-fabricated cesium lead halide perovskites.<sup>[12–16]</sup>

In this study, a layerwise vacuum deposition, which is considerably more difficult to be implemented from the solution process, was implemented to develop a perovskite active film with a thousand deposited layers.<sup>[17,18]</sup> Figure 1a shows 2D and 3D perovskite structures, which can be regarded as the iteratively stacked cesium or organic cations and  $\text{PbX}_6^{4-}$  octahedrons. Therefore, perovskite crystals can be epitaxially grown by slowly

and iteratively layering cesium or organic cations and  $\text{PbX}_6^{4-}$ . However, strict epitaxy involves applying an ultrahigh vacuum of  $10^{-9}$ – $10^{-10}$  torr and confers an extremely low growth rate, which may not be feasible for the rapid fabrication required for some optoelectronic applications, such as large-area photovoltaics. Therefore, layer-by-layer deposited perovskites was approximated using this carefully designed and rapid alternative vacuum deposition process. Although the process was conducted at a much higher pressure ( $10^{-6}$  torr) and deposition speed was controlled at a much higher rate (several Armstrong per second), a distinct morphology was revealed compared with that achieved by codeposition and multilayer alternative deposition. The films were implemented in all vacuum-deposited perovskite solar cells. The optimal performance was observed for samples with alternative layer thicknesses and the approximated theoretical cesium halide and lead halide layer thicknesses in a perovskite crystal lattice. The highest power conversion efficiency (PCE) was 13.0%, which was better than the highest PCE of 11.8% with codeposited  $\text{CsPbI}_2\text{Br}$  in our previous study.<sup>[13]</sup>

## 2. Results and Discussion

Figure 1b shows the schematic of the alternative deposition method. A baffle was used to divide the vacuum chamber into two equal parts, and a sample holder was rotated directly above the baffle. When the sample holder was rotating, two precursors could be alternatively deposited on the substrate under high vacuum. The thickness of each layer was controlled by adjusting the deposition rate of each precursor together with

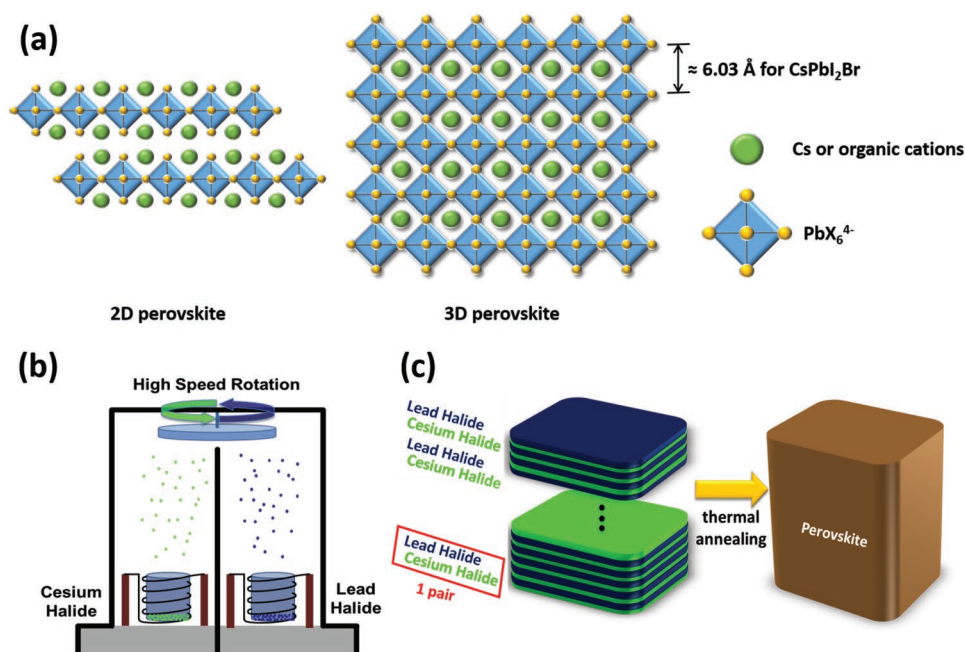


**Figure 1.** a) Schematic of 2D and 3D perovskite structures. b) Schematic of the Cs-based perovskite alternative deposition process. c) Illustration of perovskite formation through alternative deposition.

the rotation speed of the sample holder. To fabricate a  $\text{CsPbI}_2\text{Br}$  perovskite thin film,  $\text{CsBr}$  and  $\text{PbI}_2$  were used as precursors, and both materials were simultaneously evaporated in the two parts of vacuum chamber, layer by layer. After the precursor deposition was conducted, the films were annealed to be transferred to perovskite (Figure 1c). While during our previous coevaporation process, the thickness sensor near the substrate holder monitors the deposition rates of both precursors simultaneously. Hence, the crystal thickness monitor senses the total deposition rate, which makes it difficult to distinguish which precursors was the one deviating from the desired deposition rate when the total deposition rate fluctuates. In contrast, in the alternative deposition process, due to the separation of the half-chamber, the thickness sensors are able to monitor the individual deposition rates of both precursors. Therefore, the composition of  $\text{CsPbI}_2\text{Br}$  could be controlled more easily and precisely by alternative process.

For simplicity, each layer of  $\text{CsBr}$  and  $\text{PbI}_2$  were first defined as pairs. For perovskite samples of the same thickness, the more pairs there were, the thinner each pair was. Thin films with 4, 50, 660, and 1560 pairs of  $\text{CsBr}$  and  $\text{PbI}_2$  were fabricated while maintaining the total thickness of perovskite at 400 nm. Furthermore, for 660 pairs, each layer of  $\text{CsBr}$  and  $\text{PbI}_2$  was  $\approx 0.37$  and  $0.24$  nm thick, respectively, which imitated the thicknesses of  $\text{CsBr}$  and  $\text{PbI}_2$  in the  $\text{CsPbI}_2\text{Br}$  perovskite unit cell (Figure 1a).<sup>[19]</sup> The films were then annealed at  $260^\circ\text{C}$  to ensure that  $\text{CsBr}$  and  $\text{PbI}_2$  reacted and were completely transferred to a black perovskite phase.<sup>[13]</sup> Figure 2 shows the absorption spectra of the  $\text{CsPbI}_2\text{Br}$  thin films. An as-deposited film of 4 pairs exhibited a yellow appearance before annealing. The remainder of the as-deposited films of 50-, 660-, and 1560-pair samples were perovskite samples that were dark-brown in appearance with black-phase absorption after vacuum

deposition when the substrates were maintained at room temperature upon evaporation. The distinct absorption characteristic of the 4-pair sample was attributed to a large separation of 50 nm between each layer and solid-state reaction length for  $\text{CsBr}$  and  $\text{PbI}_2$  to react with perovskite is considerably smaller than 50 nm. By contrast, the as-deposited films of 50-, 660-, and 1560-pair samples with a shorter spacing between each layer formed in situ dark-brownish perovskite during deposition. After being annealed at  $260^\circ\text{C}$  for 1 min, all films exhibited the same absorbance, with an absorption onset at  $\approx 670$  nm, which corresponded with  $\text{CsPbI}_2\text{Br}$  absorption using other methods in the literature.<sup>[19–22]</sup> Moreover, the annealing time of a 660-pair sample ranged from 30 s to 10 min, and a change in absorption was observed. For an annealing time of longer than 3 min, the absorption of perovskite thin films slightly decreased (Figure S1, Supporting Information).

To evaluate the effect of different pairs of  $\text{CsBr}$  and  $\text{PbI}_2$  in this rapid alternative deposition method on device performance, active perovskite layers were integrated with all vacuum-deposited solar cell structures. The device configuration was as follows:  $\text{ITO}/\text{Ca}/\text{C}_{60}/\text{CsPbI}_2\text{Br}/\text{TAPC}/\text{TAPC}:\text{MoO}_3/\text{MoO}_3/\text{Ag}$ . Figure 3 shows the current density–voltage characteristics associated with the optimal performance for each condition and the corresponding EQE spectra. The 660-pair device exhibited optimal performance among all conditions. The 660-pair  $\text{CsPbI}_2\text{Br}$  solar cell showed a high PCE of 13.0%, with an open-circuit voltage ( $V_{\text{OC}}$ ), short-circuit current density ( $J_{\text{SC}}$ ), and fill factor (FF) of 1.13 V,  $15.6 \text{ mA cm}^{-2}$ , and up to 0.74, respectively. The optimal 1560-pair  $\text{CsPbI}_2\text{Br}$  solar cell exhibited a considerably low PCE of 9.8%, with a  $V_{\text{OC}}$ ,  $J_{\text{SC}}$ , and FF of 1.01 V,  $15.1 \text{ mA cm}^{-2}$ , and 0.64, respectively. The devices with much fewer pairs of  $\text{CsBr}$  and  $\text{PbI}_2$  (50 and 4 pairs, respectively) exhibited evident  $J$ – $V$  kink characteristics. The optimal

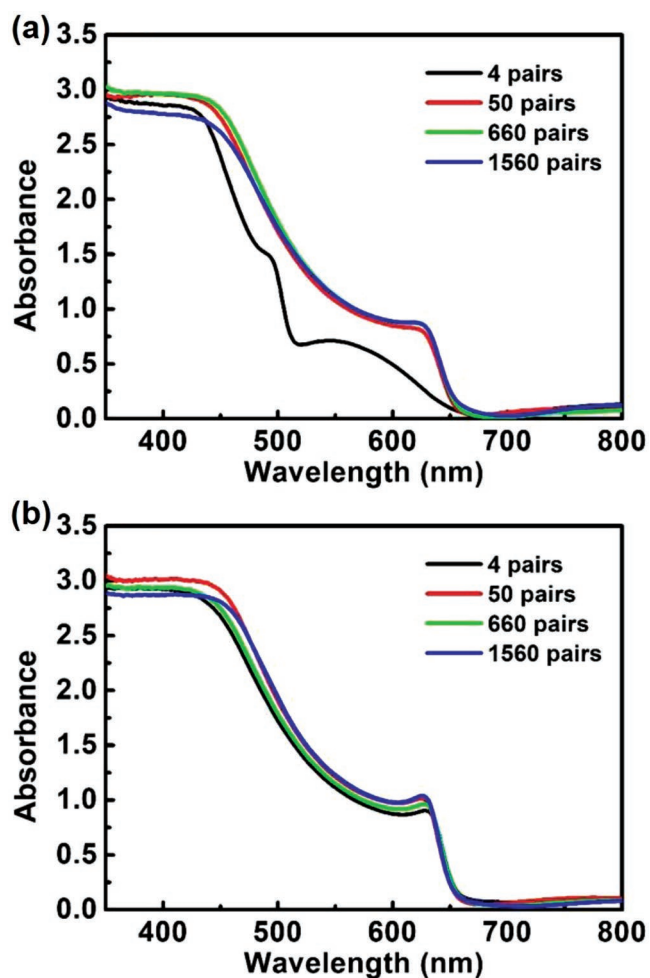


**Figure 2.** Absorbance spectra of a) as-deposited CsPbI<sub>2</sub>Br thin films with various pair numbers of b) CsBr and PbI<sub>2</sub> and films annealed at 260 °C for 1 min.

50-pair solar cell exhibited a low PCE of 8.4%, with a  $V_{OC}$  of 1.11 V, a  $J_{SC}$  of 14.6 mA cm<sup>-2</sup>, and a FF of 0.52, and the 4-pair solar cell yielded the lowest PCE of 6.6%, with a  $V_{OC}$  of 1.06 V, a  $J_{SC}$  of 12.8 mA cm<sup>-2</sup>, and a FF of 0.49. Figure S2 (Supporting Information) shows the current density–voltage characteristics of 4-, 50-, 660-, and 1560-pair CsPbI<sub>2</sub>Br devices with various annealing times. Table 1 and Tables S1–S4 (Supporting Information) summarize the performance of all devices. The comparison of the device performance between alternative and coevaporation process is summarized in Table S5 (Supporting Information). Although all films had similar absorption spectra after proper thermal annealing, all devices with different pairs of alternative layers exhibited distinct photovoltaic performance. Therefore, some factors, apart from absorption, may also affect the performance of photovoltaic devices.

To further examine the morphology of the CsPbI<sub>2</sub>Br thin films with different numbers of pairs, scanning electron microscopy (SEM) analyses were performed, and Figure 4a,b shows the results. After annealing was conducted, the 4-pair thin film exhibited abnormally small particles on the surface. With an increasing in the number of pairs, the particles

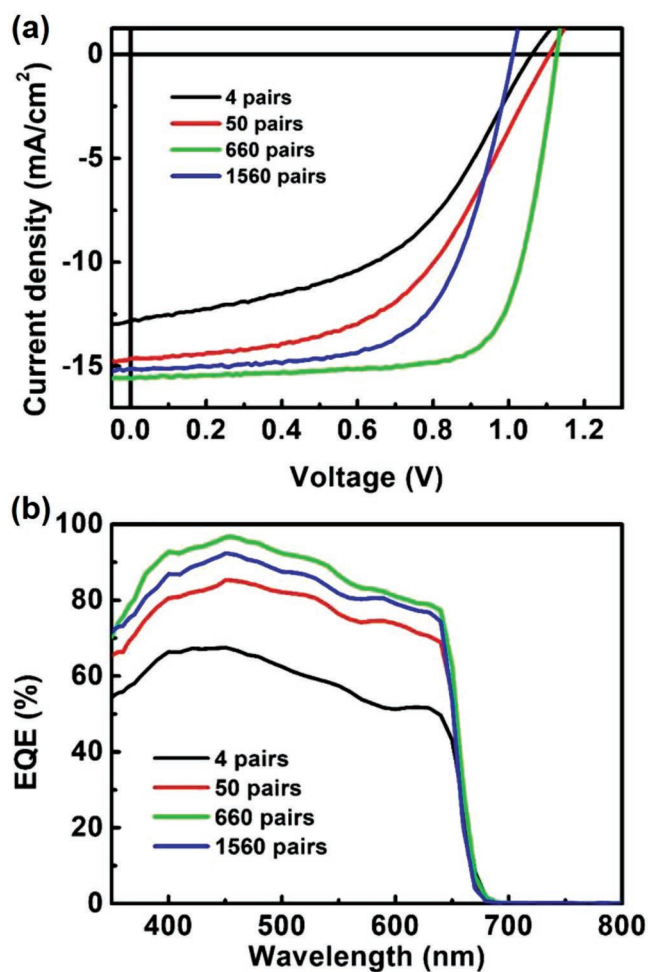


**Figure 3.** a)  $J$ - $V$  characteristics of CsPbI<sub>2</sub>Br perovskite solar cells with various pair numbers of CsBr and PbI<sub>2</sub> under 1 sun AM 1.5G illumination. b) Corresponding EQE spectra of the devices.

vanished, and the films had a size of several hundred nanometers. The 660- and 1560-pair thin films exhibited an equal number of bright and black domains, which may be attributed to composition or the geometric (height) differences of each domain. To examine the composition of light and dark domains in an SEM image of 660-pair thin films, energy-dispersive X-ray (EDS) mapping was performed. Figure 4c shows the EDS results of Cs, Pb, I, and Br. No compositional difference was observed between light and dark domains. Therefore, color differences in the SEM image were attributed to the different heights of these domains. This argument is supported by

**Table 1.** Performance of CsPbI<sub>2</sub>Br solar cells with various numbers of CsBr and PbI<sub>2</sub> pairs.

	$V_{OC}$ [V]	$J_{SC}$ [mA cm <sup>-2</sup> ]	FF	PCE [%]
4-pairs	1.06	12.8	0.49	6.6
50-pairs	1.11	14.6	0.52	8.4
660-pairs	1.13	15.6	0.74	13.0
1560-pairs	1.01	15.1	0.64	9.8

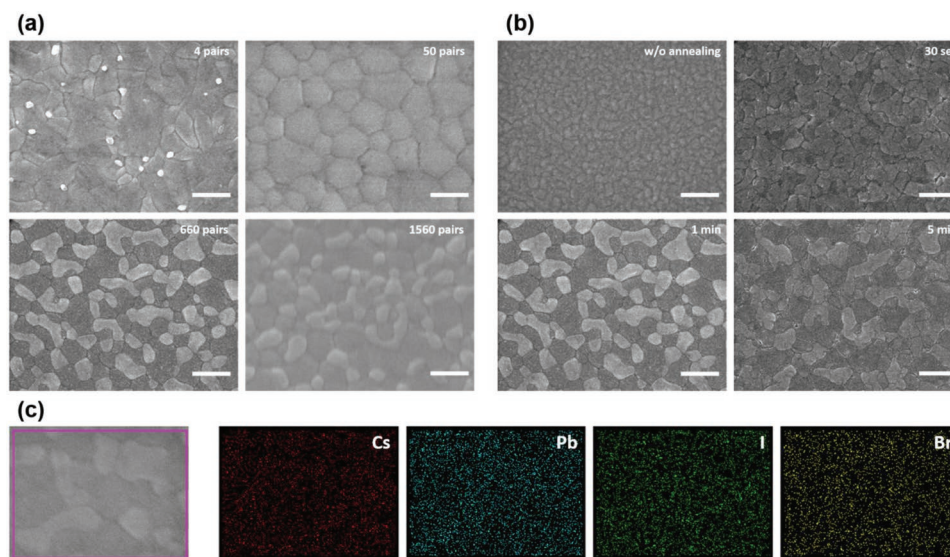


**Figure 4.** Top-view SEM images of a) CsPbI<sub>2</sub>Br thin films with various pair numbers of CsBr and PbI<sub>2</sub> annealed at 260 °C for 1 min and b) 660-pair CsPbI<sub>2</sub>Br thin films annealed for different times at 260 °C. Scale bar: 2 μm. c) EDS mapping images of 660-pair CsPbI<sub>2</sub>Br thin films.

atomic force microscopy (AFM) images (Figure S3, Supporting Information), which provided thin-film surface topography. As for the rougher surfaces for 660-pair and 1560-pair thin films compared to the 4-pair and 50-pair ones, we believed that it was because of the more uniform mixing and reaction of the cesium halide and lead halide during the deposition, leading to a larger number of nucleation and growth centers during the subsequent thermal annealing. The larger number of nucleation and growth centers made them exhibit rougher surface morphologies after the samples were subjected to a thermal annealing for the same period of time.

Figure 5a,b,d,e shows the 2D grazing-incidence wide-angle X-ray scattering (GIWAXS) patterns of the 4- and 660-pair films with and without thermal annealing at 260 °C, thus revealing the evolution of the structure and orientation of film crystallites

prepared using these two processes. The as-deposited films of the 4-pair sample exhibited preferred crystal orientation in an out-of-plane direction (normal for a substrate), which was attributed to PbI<sub>2</sub> crystallites and was consistent with the absorption spectrum of the sample.<sup>[23]</sup> By contrast, the film of a 660-pair sample had weak isotropic crystallites. After annealing, the two samples exhibited evident diffraction signals. Figure 5c,f shows the ring-averaged GIWAXS profiles reduced from the 2D GIWAXS patterns of the films. The GIWAXS intensities of the films without annealing treatment were considerably weaker than those subjected to annealing treatment, thus exhibiting low crystallinity. This study focused on the GIWAXS profiles of the annealed film. The GIWAXS profiles of the 4-pair annealed film were similar to the obtained X-ray diffraction (XRD) data of the cubic CsPbI<sub>3</sub> perovskite phase at high temperatures.<sup>[21]</sup>

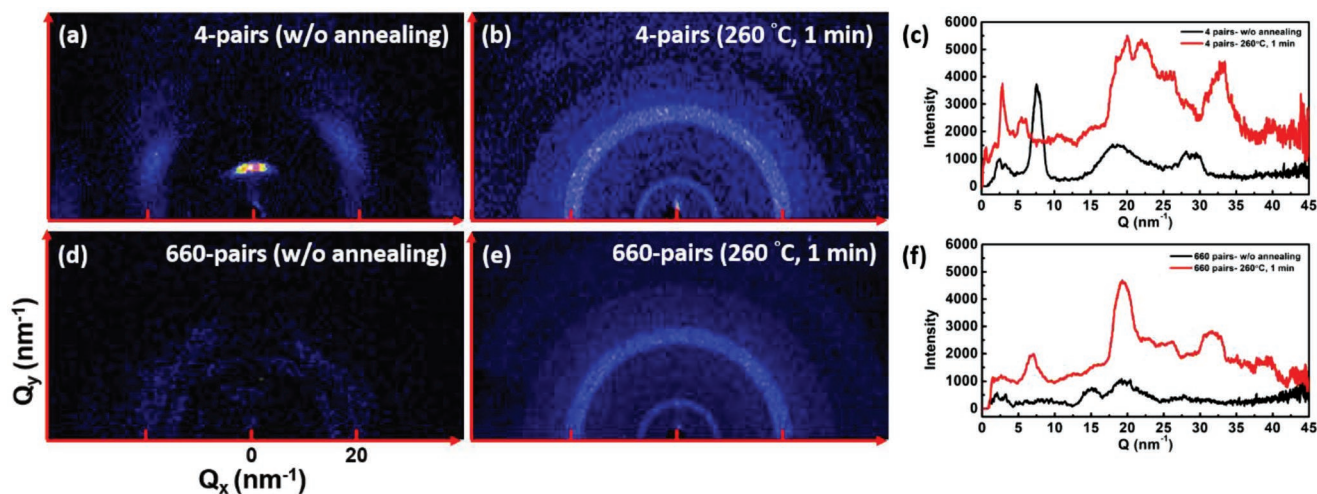


**Figure 5.** 2D GIWAXS patterns of a) a 4-pair as-deposited film, b) films annealed at 260 °C for 1 min, d) a 660-pair as-deposited film, e) films annealed at 260 °C for 1 min. c,f) Derived from the azimuthal ring average of (a), (b), (d), and (e).  $Q_x$  is along the in-plane direction (parallel to the film surface), whereas  $Q_y$  is along the out-of-plane direction (normal to the film surface).

According to the calculated XRD data, the peaks appeared at a scattering vector of approximately 10, 14.2, 20, and 28.5 nm<sup>-1</sup> ( $Q = 4\pi/\lambda \cdot \sin\theta$ , where  $\theta$  is the diffraction angle;  $2\theta \approx 14^\circ, 20^\circ, 28^\circ, \text{ and } 42^\circ$ ). The highest intensity peak (200) was close to  $Q = 20 \text{ nm}^{-1}$  for all CsPbI<sub>3</sub> perovskite (cubic and orthorhombic) and CsPbI<sub>2</sub>Br phases. The obtained GIWAXS profile was slightly different from the calculated XRD of the cubic CsPbI<sub>3</sub> perovskite phase because of the effect of bromide on the lattice and the lattice disordering of interstitial atoms from the phase transition. By contrast, the GIWAXS profile of the 660-pair annealed film was similar to that of the CsPbI<sub>2</sub>Br phase. The (100) peak deviated from the prediction value ( $Q = 10 \text{ nm}^{-1}$ ), which could be attributed to the bromide content or the effect of the annealing temperature.

For thin films made by few CsBr and PbI<sub>2</sub> pairs, the thicknesses of the CsBr and PbI<sub>2</sub> layers were too thick that CsBr and PbI<sub>2</sub> need to diffuse long distances to form CsPbI<sub>2</sub>Br during the thermal annealing. Moreover, there were more chances for these CsPbI<sub>2</sub>Br thin films to contain undesired Cs-rich phase, that is, Cs<sub>4</sub>PbX<sub>6</sub>, in the thin film, which was formed when only trace PbI<sub>2</sub> diffused into CsBr layers and reacted with CsBr during the early stage of the thermal annealing.<sup>[24]</sup> The lattice spacing of Cs<sub>4</sub>PbX<sub>6</sub> matches that of the multiple CsPbX<sub>3</sub>, making Cs<sub>4</sub>PbX<sub>6</sub> difficult to be converted to CsPbX<sub>3</sub>.<sup>[24]</sup> Therefore, we believe that the CsPbI<sub>2</sub>Br device made with more pairs exhibits higher PCEs due to the more homogeneous mixing of the CsBr and PbI<sub>2</sub> precursors in the as-deposited thin films, which agrees well with the results of 4-, 50-, and 660-pair CsPbI<sub>2</sub>Br devices. However, the PCE of the device dropped when CsBr and PbI<sub>2</sub> was further increased to 1560 pairs. The lower PCE mainly

came from the lower  $V_{OC}$  compared to that of the 660-pair samples. We hypothesized that the CsBr and PbI<sub>2</sub> mixed and reacted more uniformly and completely in the 1560-pair samples than that of the 660-pair ones during the deposition, leading to a larger number of nucleation and growth centers and thus a rougher surface after a thermal annealing. The rougher surface of the 1560-pair CsPbI<sub>2</sub>Br made it more possible for the metal electrode and the MoO<sub>3</sub> in the doped HTLs to contact CsPbI<sub>2</sub>Br active layer, which lead to an increased carrier recombination loss and the lower PCE and  $V_{OC}$  of the devices.<sup>[25]</sup> To support this hypothesis, we performed AFM measurement on the 1560-pair CsPbI<sub>2</sub>Br thin film. As shown in Figure S4 (Supporting Information), the 1560-pair CsPbI<sub>2</sub>Br did exhibit a higher  $R_q$  of 24.1 nm than that of the 660-pair CsPbI<sub>2</sub>Br (14 nm, as shown in Figure S3, Supporting Information). The results support our hypothesis that the lower PCE and  $V_{OC}$  of the 1560-pair device were due to the higher surface roughness and probably a higher carrier recombination in the device. In short, it suggests that the processing conditions of the alternative-deposited perovskites need to strike a balance between the surface roughness, which is determined by the number of the crystal growth centers, and solid state diffusion length, which determined the perovskite quality.

The 660-pair CsPbI<sub>2</sub>Br device not only showed the highest performance among all conditions but also delivered a stabilized efficiency of 12.8%, which was similar to the previous  $J-V$  sweeping results (Figure 6a). With different scanning directions, the device exhibited negligible hysteresis in  $J-V$  characteristics (Figure 6b). Table 2 summarizes the performances of the device in different scanning directions. In the long-term

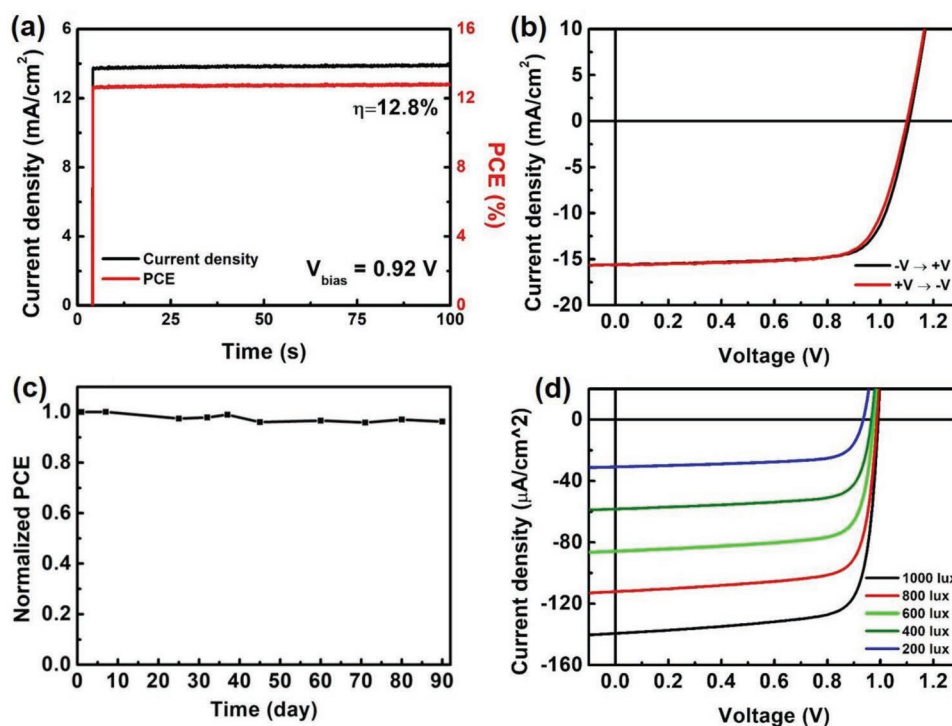


**Figure 6.** a) Photocurrent density and PCE as functions of time of the optimal CsPbI<sub>2</sub>Br solar cell at a bias of 0.92 V. b)  $J-V$  characteristics of the optimal CsPbI<sub>2</sub>Br perovskite solar cell measured in different scanning directions under 1 sun AM 1.5 G illumination. c) Long-term PCE stability of the 660-pair CsPbI<sub>2</sub>Br solar cell. d)  $J-V$  characteristics of the optimal CsPbI<sub>2</sub>Br solar cell measured under fluorescent lamp illumination of 600 lux.

**Table 2.** Photovoltaic parameters of the optimal CsPbI<sub>2</sub>Br solar cell in different scan directions.

Scan direction	V <sub>OC</sub> [V]	J <sub>SC</sub> [mA cm <sup>-2</sup> ]	FF	PCE [%]
-V → +V	1.11	15.6	0.74	12.9
+V → -V	1.10	15.6	0.74	12.6

stability test, the device maintained 96% of its optimal efficiency with encapsulation for 90 d (Figure 6c). It is worth mentioning that although the vacuum deposited CsPbI<sub>2</sub>Br thin films exhibited a good stability with an encapsulation, but they easily degrade at an ambient condition. The Figure S5a (Supporting Information) shows the evolution of the alternative deposited CsPbI<sub>2</sub>Br thin film in an ambient condition (RH ≈ 60%). It can be seen that CsPbI<sub>2</sub>Br thin films started to degrade in an ambient condition in 90 s and totally converted to a transparent appearance in 270 s. The degradation of the CsPbI<sub>2</sub>Br thin film in an ambient condition with a reduced humidity was also investigated. The Figure S5b (Supporting Information) displays the evolution of a CsPbI<sub>2</sub>Br thin film in a dry box (RH ≈ 35%). The thin film showed a retarded degradation compared to the one stored in a RH ≈ 60% ambient condition but eventually turned into a transparent appearance in 20 min. We believe that the quick degradation in an ambient condition is the intrinsic nature of the CsPbI<sub>2</sub>Br thin film and the stability of CsPbI<sub>2</sub>Br devices can be largely extended with proper encapsulation.

The large E<sub>g</sub> of CsPbI<sub>2</sub>Br also makes it a promising light harvesting material in artificial light environments.<sup>[26,27]</sup> Under a fluorescent light illumination of 1000 lux, the device delivered a high PCE of 33.9%. Figure 6d shows the J–V characteristics of the 660-pair CsPbI<sub>2</sub>Br device under fluorescent light illumination and the spectrum of indoor light is shown in Figure S6 (Supporting Information). Table S6 (Supporting Information) summarizes the performance of the devices.

### 3. Conclusion

In summary, the alternative deposition provides new approaches for Cs-based perovskite fabrication, and the implementation of this method is more difficult than that of the solution process. Moreover, layer-by-layer fabrication can be obtained by precisely controlling the thickness of each layer in an alternative vacuum deposition process without substantially sacrificing the fabrication speed. The 660-pair CsPbI<sub>2</sub>Br thin film exhibited a smooth surface and high crystallinity, and the solar cell device delivered the highest PCE of 13.0%, with a V<sub>OC</sub> of 1.13 V, a J<sub>SC</sub> of 15.6 mA cm<sup>-2</sup>, and a FF of up to 0.74. Furthermore, the device had a stabilized efficiency of 12.8%, which was similar to the J–V sweeping results. Furthermore, the use of these devices for environmental light energy harvesting was validated by a PCE of 33.9% under fluorescent light illumination of 1000 lux. The device maintained 96% of its performance with encapsulations for 90 d. The process used in this study not only demonstrated a new method for efficient perovskite solar cell fabrication but also provided a novel approach for obtaining widely applicable high-quality perovskite thin films for various optoelectronic devices.

### 4. Experimental Section

**Device Fabrication:** The devices were prepared on cleaned indium tin oxide (ITO) substrates. The substrates were maintained at room temperature and were loaded into a high-vacuum chamber (a base pressure of ≈2 × 10<sup>-6</sup> torr) to deposit layers of Ca, C<sub>60</sub>, and perovskite. For four-pair CsPbI<sub>2</sub>Br thin films and devices, PbI<sub>2</sub> and CsBr were alternatively deposited with a thickness of 60.9 and 39.1 nm four times. For 50-pair CsPbI<sub>2</sub>Br thin films and devices, PbI<sub>2</sub> and CsBr were deposited at a rate of 0.98 and 0.64 Å s<sup>-1</sup>, respectively, with the sample holder rotating at 1.2 rpm. For 660-pair CsPbI<sub>2</sub>Br thin films and devices, PbI<sub>2</sub> and CsBr were deposited at the rate of 0.92 and 0.59 Å s<sup>-1</sup>, respectively, with the sample holder rotating at 15 rpm. For 1560-pair CsPbI<sub>2</sub>Br thin films and devices, PbI<sub>2</sub> and CsBr were deposited at a rate of 0.78 and 0.5 Å s<sup>-1</sup>, respectively, with the sample holder rotating at 30 rpm. During alternative deposition, the deposition rate was monitored using quartz crystal microbalance sensors. After the deposition of PbI<sub>2</sub> and CsBr, the samples were annealed at 260 °C in an anhydrous nitrogen atmosphere. After thermal annealing was complete, the samples were transferred back to a high-vacuum chamber for 4,4-cyclohexylidenebis[N,N-bis(4-methylphenyl)benzenamine] (TAPC), TAPC:MoO<sub>3</sub> (65:35, v/v), MoO<sub>3</sub>, and Ag depositions. The devices were configured as a glass substrate/ITO (145 nm)/Ca (1 nm)/C<sub>60</sub> (5–15 nm)/CsPbI<sub>2</sub>Br (400 nm)/TAPC (10 nm)/TAPC:MoO<sub>3</sub> (120 nm)/MoO<sub>3</sub> (10 nm)/Ag (150 nm). The device areas (0.051 cm<sup>2</sup>) were defined using shadow masks. The devices were encapsulated using an ultraviolet (UV)-cured sealant (Everwide Chemical Co.) and cover glasses after fabrication, and they were subsequently characterized in air.

**Device Measurement and Characterization:** SEM images were obtained using a Hitachi SU8010 field-emission SEM. ITO/Ca/C<sub>60</sub>-coated glasses were used as substrates. The thicknesses of the ITO, Ca, and C<sub>60</sub> devices were 145, 1, and 5 nm, respectively. For the SEM measurements, the samples were prepared under the same conditions as those used for device fabrication. The samples were transferred to a vacuum chamber and rapidly loaded into an SEM antechamber to reduce air exposure time to ≈10 s. For GIWAXS measurements, film specimens with an area of 2 × 2 cm<sup>2</sup> were deposited on Ca/C<sub>60</sub>-coated Si substrates. The thicknesses of the Ca and C<sub>60</sub> films were 1 and 5 nm, respectively. The samples were rapidly loaded into a GIWAXS instrument to reduce air exposure time to ≈30 s. The GIWAXS experiments were conducted with a collection time of 30 min by using a Bruker instrument (AXS GmbH, Nanostar) operated at 2.5 kW (50 kV, 50 mA) at room temperature in a vacuum. The GIWAXS instrument possessed a well-collimated system and a 2D image plate detector with an area of 20 × 25 cm<sup>2</sup>. Silver behenate powder was used as the standard sample for calibration. The absorption spectra were acquired using a Shimadzu UV-2600 spectrophotometer, and the samples were encapsulated using a UV-cured sealant and cover glasses. The J–V characteristics of the devices were measured using a Keithley 2636B SourceMeter in the dark under AM 1.5G simulated solar illumination with an intensity of 100 mW cm<sup>-2</sup> (1 sun, calibrated by an NREL-traceable KG5 filtered silicon reference cell) and under a 6500-K color temperature Philips T5 fluorescent lamp. The irradiance and luminance of the T5 fluorescent lamp were determined using an NIST-traceable Ophir radiometer (PD300-BB-50 mW) and a photometer (PD300-CIE), respectively. The scan direction was generally considered from a positive to negative bias, with a step size of 10 mV and a delay time between points of 300 ms. The EQE spectra were obtained by illuminating the solar cells with chopped monochromatic light and a continuous-wave bias white light (from a halogen lamp). The photocurrent signals were extracted using the lock-in technique through the use of a Stanford Research System current preamplifier and an Ametek lock-in amplifier. The intensity of the monochromatic light was calibrated with an NIST-traceable Ophir power meter. A device stability test was performed with UV-epoxy encapsulated cells. The cells were stored in a dark environment at room temperature (≈25 °C) and regularly measured under AM 1.5G, 1 sun, simulated solar illumination. The J–V sweeping direction was considered from a positive to negative bias, with a step size of 10 mV and a delay time between points of 300 ms.

## Supporting Information

Supporting Information is available from the Wiley Online Library or from the author.

## Acknowledgements

The authors acknowledge the financial support from the Ministry of Science and Technology of Taiwan (Grant No. 108-2636-E-007-012), National Tsing Hua University.

## Conflict of Interest

The authors declare no conflict of interest.

## Keywords

alternative deposition, cesium, perovskite solar cells, vacuum deposition

Received: June 27, 2019

Revised: July 26, 2019

Published online: August 16, 2019

- [1] H. Cho, S.-H. Jeong, M.-H. Park, Y.-H. Kim, C. Wolf, C.-L. Lee, J. H. Heo, A. Sadhanala, N. Myoung, S. Yoo, S. H. Im, R. H. Friend, T.-W. Lee, *Science* **2015**, 350, 1222.
- [2] J. Gong, S. B. Darling, F. You, *Energy Environ. Sci.* **2015**, 8, 1953.
- [3] H.-S. Kim, C.-R. Lee, J.-H. Im, K.-B. Lee, T. Moehl, A. Marchioro, S.-J. Moon, R. Humphry-Baker, J.-H. Yum, J. E. Moser, M. Grätzel, N.-G. Park, *Sci. Rep.* **2012**, 2, 591.
- [4] Y.-H. Kim, H. Cho, J. H. Heo, T.-S. Kim, N. Myoung, C.-L. Lee, S. H. Im, T.-W. Lee, *Adv. Mater.* **2015**, 27, 1248.
- [5] A. Kojima, K. Teshima, Y. Shirai, T. Miyasaka, *J. Am. Chem. Soc.* **2009**, 131, 6050.
- [6] N.-G. Park, *Mater. Today* **2015**, 18, 65.
- [7] G. Xing, N. Mathews, S. S. Lim, N. Yantara, X. Liu, D. Sabba, M. Grätzel, S. Mhaisalkar, T. C. Sum, *Nat. Mater.* **2014**, 13, 476.
- [8] C.-W. Chen, H.-W. Kang, S.-Y. Hsiao, P.-F. Yang, K.-M. Chiang, H.-W. Lin, *Adv. Mater.* **2014**, 26, 6647.
- [9] S.-Y. Hsiao, H.-L. Lin, W.-H. Lee, W.-L. Tsai, K.-M. Chiang, W.-Y. Liao, C.-Z. Ren-Wu, C.-Y. Chen, H.-W. Lin, *Adv. Mater.* **2016**, 28, 7013.
- [10] M. Liu, M. B. Johnston, H. J. Snaith, *Nature* **2013**, 501, 395.
- [11] O. Malinkiewicz, A. Yella, Y. H. Lee, G. M. Espallargas, M. Graetzel, M. K. Nazeeruddin, H. J. Bolink, *Nat. Photonics* **2014**, 8, 128.
- [12] P. Becker, J. A. Márquez, J. Just, A. Al-Ashouri, C. Hages, H. Hempel, M. Jošt, S. Albrecht, R. Frahm, T. Unold, *Adv. Energy Mater.* **2019**, 9, 1900555.
- [13] C.-Y. Chen, H.-Y. Lin, K.-M. Chiang, W.-L. Tsai, Y.-C. Huang, C.-S. Tsao, H.-W. Lin, *Adv. Mater.* **2017**, 29, 1605290.
- [14] J. Lei, F. Gao, H. Wang, J. Li, J. Jiang, X. Wu, R. Gao, Z. Yang, S. Liu, *Sol. Energy Mater. Sol. Cells* **2018**, 187, 1.
- [15] H. Li, G. Tong, T. Chen, H. Zhu, G. Li, Y. Chang, L. Wang, Y. Jiang, *J. Mater. Chem. A* **2018**, 6, 14255.
- [16] Q. Ma, S. Huang, X. Wen, M. A. Green, A. W. Y. Ho-Baillie, *Adv. Energy Mater.* **2016**, 6, 1502202.
- [17] J. W. Kim, H. J. Kim, H. H. Lee, T. Kim, J.-J. Kim, *Adv. Funct. Mater.* **2011**, 21, 2067.
- [18] M. Shahiduzzaman, K. Yonezawa, K. Yamamoto, T. S. Ripolles, M. Karakawa, T. Kuwabara, K. Takahashi, S. Hayase, T. Taima, *ACS Omega* **2017**, 2, 4464.
- [19] R. E. Beal, D. J. Slotcavage, T. Leijtens, A. R. Bowering, R. A. Belisle, W. H. Nguyen, G. F. Burkhard, E. T. Hoke, M. D. McGehee, *J. Phys. Chem. Lett.* **2016**, 7, 746.
- [20] C. F. J. Lau, M. Zhang, X. Deng, J. Zheng, J. Bing, Q. Ma, J. Kim, L. Hu, M. A. Green, S. Huang, A. Ho-Baillie, *ACS Energy Lett.* **2017**, 2, 2319.
- [21] R. J. Sutton, G. E. Eperon, L. Miranda, E. S. Parrott, B. A. Kamino, J. B. Patel, M. T. Hörantner, M. B. Johnston, A. A. Haghghirad, D. T. Moore, H. J. Snaith, *Adv. Energy Mater.* **2016**, 6, 1502458.
- [22] J. Zhang, D. Bai, Z. Jin, H. Bian, K. Wang, J. Sun, Q. Wang, S. Liu, *Adv. Energy Mater.* **2018**, 8, 1703246.
- [23] Y.-C. Huang, C.-S. Tsao, Y.-J. Cho, K.-C. Chen, K.-M. Chiang, S.-Y. Hsiao, C.-W. Chen, C.-J. Su, U. S. Jeng, H.-W. Lin, *Sci. Rep.* **2015**, 5, 13657.
- [24] L. N. Quan, R. Quintero-Bermudez, O. Voznyy, G. Walters, A. Jain, J. Z. Fan, X. Zheng, Z. Yang, E. H. Sargent, *Adv. Mater.* **2017**, 29, 1605945.
- [25] P. Schulz, J. O. Tjepelt, J. A. Christians, I. Levine, E. Edri, E. M. Sanehira, G. Hodes, D. Cahen, A. Kahn, *ACS Appl. Mater. Interfaces* **2016**, 8, 31491.
- [26] C.-Y. Chen, J.-H. Chang, K.-M. Chiang, H.-L. Lin, S.-Y. Hsiao, H.-W. Lin, *Adv. Funct. Mater.* **2015**, 25, 7064.
- [27] C.-Y. Chen, W.-H. Lee, S.-Y. Hsiao, W.-L. Tsai, L. Yang, H.-L. Lin, H.-J. Chou, H.-W. Lin, *J. Mater. Chem. A* **2019**, 7, 3612.